

## Supporting Information

### Facet engineering of cobalt manganese oxide for highly stable acidic oxygen evolution reaction

Chi Wing Lee<sup>1</sup>, Claudio Cazorla<sup>2</sup>, Shujie Zhou<sup>1,\*</sup>, Ding Zhang<sup>1</sup>, Hanyu Xu<sup>1</sup>, Wenyu Zhong<sup>1</sup>, Ming Zhang<sup>1</sup>, Dewei Chu,<sup>3</sup> Zhaojun Han<sup>1,4,\*</sup>, Rose Amal<sup>1</sup>

<sup>1</sup> School of Chemical Engineering, The University of New South Wales, Kensington, NSW 2052, Australia

<sup>2</sup> Department of Physics, Polytechnic University of Catalonia (UPC), 08034 Barcelona, Spain

<sup>3</sup> School of Materials Science and Engineering, The University of New South Wales, Kensington, NSW 2052, Australia

<sup>4</sup> School of Mechanical, Medical and Process Engineering, Queensland University of Technology, Brisbane, QLD 4000, Australia

\*CORRESPONDING AUTHOR

shujie.zhou@unsw.edu.au

zhaojun.han@qut.edu.au

## **Experimental Section**

### ***Materials***

Cobalt(II) nitrate hexahydrate (98%), Nickel(II) nitrate hexahydrate (97.0%), Manganese nitrate tetrahydrate (97.0%), Cobalt(II,III) oxide (99.5%), Cobalt(II) oxide (99.5%), Nickel(II) oxide (99.99%), Manganese(II) oxide (99%), and Manganese(IV) oxide (99%) were acquired from Sigma-Aldrich. Platinized titanium (Pt/Ti) fiber felt, titanium fiber felt, and 20% Platinum on Carbon XC-72 were sourced from Fuel Cell Store. Sulfuric acid (H<sub>2</sub>SO<sub>4</sub>) was obtained from Chem-Supply.

### ***Fabrication of pristine and Ni-doped cobalt manganese on Pt/Ti fiber felt***

A piece of Pt/Ti felt measuring 2 x 1 cm<sup>2</sup> was meticulously cleaned through a sonication process using ethanol, isopropyl alcohol, and deionized water (DI) sequentially for 5 minutes each.

*Co<sub>2</sub>MnO<sub>4</sub>*: To prepare the precursor solution, cobalt nitrate hexahydrate (Co(NO<sub>3</sub>)<sub>2</sub>·6H<sub>2</sub>O) and manganese nitrate tetrahydrate (Mn(NO<sub>3</sub>)<sub>2</sub>·4H<sub>2</sub>O) were dissolved in DI water to achieve a total concentration of 2.5 M, maintaining a molar ratio of Co to Mn at 2:1. Subsequently, 30 μL of this precursor solution was precisely dropped onto the Pt/Ti felt substrate (an exposed geometric surface area of 1 cm<sup>2</sup>). This was followed by a calcination process in a muffle furnace at 300°C in an air atmosphere, sustained for 12 hours. Post-calcination, the electrode was briefly sonicated in DI water for 10 seconds to detach any loosely adhered catalyst particles. To ensure complete coverage of the catalyst film on the Pt/Ti felt substrate, this process of drop casting, calcination, and cleaning was repeated for a second cycle. The typical loading amount of catalyst oxide film was measured to be 10 mg cm<sup>-2</sup>.

*Ni-doped Co<sub>2</sub>MnO<sub>4</sub>*: The Ni-doped Co<sub>2</sub>MnO<sub>4</sub> was synthesized by incorporating the nickel (II) nitrate hexahydrate into the cobalt-manganese precursor solution. This addition was quantified as 'x%' molar of Ni, within the total cation concentration of 2.5 M.

*Co<sub>3</sub>O<sub>4</sub>*: The Co<sub>3</sub>O<sub>4</sub> was prepared using the same calcination process with 2.5 M of cobalt nitrate hexahydrate (Co(NO<sub>3</sub>)<sub>2</sub>·6H<sub>2</sub>O) as precursor solution.

### ***Fabrication of pristine and Ni-doped cobalt manganese powders***

The preparation method of pristine and Ni-doped cobalt manganese oxide powders involved drop-casting the above-mentioned precursor solution onto a glass slide, followed by calcination in a muffle furnace at 300 °C for 12 hours in air. The resulting thin film was then scraped off the glass slide and ground into powder for XRD analysis.

### ***Electrochemical Characterization***

Electrochemical characterizations were carried out on a Metrohm Autolab station with a three-electrode cell setup. A platinum mesh and a saturated calomel electrode (SCE) served as the counter and reference electrodes, respectively. The working electrodes were confined to an exposed area of 1 cm<sup>2</sup> using Teflon tape. Polarization curves were recorded at a 5 mV s<sup>-1</sup> scan rate with 95%  $iR_s$  compensation, and the series resistance ( $R_s$ ) was determined through electrochemical impedance spectroscopy (EIS) conducted at 1.3 V<sub>RHE</sub> from 5 kHz to 0.1 Hz with a 5-mV amplitude.

All reported potentials were converted to the reversed hydrogen electrode (RHE) reference unless otherwise specified. This conversion was performed using the Nernst equation, as described by the formula:  $E = E_{SCE} + E_{app} + 0.059 \cdot pH$ , where  $E$  represented the converted potential versus RHE,  $E_{app}$  was the experimentally applied potential versus the reference electrode, and  $E_{SCE}$  was the potential of the reference electrode relative to RHE ( $E_{SCE} \approx 0.241$  V<sub>RHE</sub>). The pH of the electrolyte was measured using a pH meter.

The electrochemically active surface area (ECSA) was determined by dividing the double layer capacitance ( $C_{dl}$ ) of the electrocatalysts by the specific capacitance ( $C_s$ ) in 0.5 M H<sub>2</sub>SO<sub>4</sub>, which was 0.035 mF cm<sup>-2</sup> for a flat surface.<sup>[1]</sup>

$$ECSA = \frac{C_{dl}}{C_s}$$

The double layer capacitance ( $C_{dl}$ ) of the electrocatalysts was assessed using cyclic voltammetry (CV) data obtained within a non-Faradaic potential window from 1.05 to 1.15 V<sub>SCE</sub>. The current densities ( $j_a$  and  $j_c$ ) from the CV curves at 1.08 V were measured at various scan rates (25, 27, 29, 31, and 33 mV s<sup>-1</sup>) and plotted against the scan rate. The slope of the appropriate linear segment of this plot was equivalent to the  $C_{dl}$  (mF cm<sup>-2</sup>).

The accelerated degradation test (ADT) was applied to determine the catalyst stability. The catalysts were scanned at different CV cycles (1<sup>st</sup>, 5000<sup>th</sup>, 15000<sup>th</sup>). Each CV cycle was conducted within a potential window ranging from 1.35 V<sub>RHE</sub> to 1.70 V<sub>RHE</sub>, allowing for a comprehensive evaluation of catalyst durability under accelerated aging conditions.

### ***Material Characterizations***

Scanning electron microscopy (SEM) and energy-dispersive x-ray spectroscopy (EDS) mapping analyses were conducted using a FEI Nova NanoSEM microscope. Transmission Electron Microscopy (TEM) imaging was performed using a JEOL JEM-F200 microscope. X-ray Diffraction (XRD) analysis was carried out utilizing a PANalytical Empyrean XRD system equipped with a Co K $\alpha$  source ( $\lambda = 1.78901 \text{ \AA}$ ) for powder samples and Cu K $\alpha$  source ( $\lambda = 1.540598 \text{ \AA}$ ) for thin film samples. The Rietveld refinement analysis was performed using HighScore Plus software. X-ray Photoelectron Spectroscopy (XPS) was conducted using a Thermo ESCALAB250i high-resolution X-ray Photoelectron with Al K $\alpha$  radiation as the X-ray source. All reported XPS spectra were calibrated by C 1s at 284.8 eV. Inductively Coupled Plasma Optical Emission Spectroscopy (ICP-OES) analysis was performed with a PerkinElmer Optima 7000 instrument.

Co, Mn, and Ni K-edge X-ray absorption spectroscopy (XAS) analyses were conducted in transmission mode at the MEX1 XAS beamline of the Australian Synchrotron. The collection of X-ray absorption near-edge structure (XANES) and extended X-ray absorption fine structure (EXAFS) data for the samples was meticulously processed using the Athena software. This involved the subtraction of pre-edge and post-edge backgrounds and normalization of the spectra against the edge height. The calibration was performed at specific  $E_0$  values corresponding to different reference foils: 7709 eV for Co, 6539 eV for Mn, and 8333 eV for Ni. Following this, the  $k^3$ -weighted EXAFS spectra were derived by removing the post-edge background from the overall absorption and then normalizing it to the edge-jump step. All curve fittings were performed in R space, with a  $k$ -weight of 3 to ensure detailed and accurate interpretation of the data.

## DFT calculations

First-principles calculations based on density functional theory (DFT) [2] were carried out with the PBEsol exchange-correlation energy functional [3] as it was implemented in the VASP software [4]. The projector-augmented wave method (PAW) [5] was employed to represent the ionic cores by considering the following electronic states as valence: Co 4s, 3d; Mn 3p, 4s, 3d; Ni 4s, 3d; O 2s, 2p. An energy cutoff of 550 eV and a dense Monkhorst-Pack k-point density equivalent to a grid of 6\*6\*6 on the cubic spinel unit cell containing 56 atoms were used for integrations within the Brillouin zone, leading to total energies converged to within less than 1 meV per atom. Atomic relaxations were concluded when the forces in all the atoms were below 0.005 eV Å<sup>-1</sup>. The supercells employed for the simulation of Co<sub>2</sub>MnO<sub>4</sub> surfaces included a large vacuum region of 25 Å height and a similar region of materials layers. In particular, the (111), (400) and (311) surface supercells contained a total of 83, 111 and 151 atoms, respectively. The “Hubbard-U” scheme according to Dudarev et al. was employed in the PBEsol calculations for a better treatment of the Co, Mn and Ni 3d electrons, adopting a U value of 2, 4 and 2 eV, respectively [6]. The Ni-doped systems were generated by performing Co-substitutions on the octahedral sites at ≈5% concentration and sampling all possible inequivalent positions. The surface formation energy,  $E_{surf}$ , was estimated with the formula:

$$E_{surf} = \frac{E_{DFT} - (N \cdot E_{bulk})}{2 \cdot S}$$

where  $E_{DFT}$  was the energy of the surface supercell directly obtained from the DFT calculations,  $E_{bulk}$  was the energy per formula unit of the corresponding bulk system, N was the number of formula units in the surface supercell, and S was the area of the surface supercell perpendicular to the vacuum direction.

Spinel oxides generally follow the formula AB<sub>2</sub>O<sub>4</sub>. In a normal spinel structure, like Co<sub>3</sub>O<sub>4</sub>, the A cations (Co<sup>2+</sup>) are located in the tetrahedral sites, while the B cations (Co<sup>3+</sup>) occupy the octahedral sites, forming the configuration [Co<sup>2+</sup>]<sup>tet</sup>[Co<sup>3+</sup>]<sub>2</sub><sup>oct</sup>O<sub>4</sub>. [7] In contrast, inverse spinel has half of the B ions in tetrahedral sites and the remaining B and A ions sharing the octahedral sites. For instance, in Fe<sub>3</sub>O<sub>4</sub>, Fe<sup>2+</sup> and half of the Fe<sup>3+</sup> ions occupy octahedral sites, with the other half of the Fe<sup>3+</sup> ions in tetrahedral sites, described as [Fe<sup>3+</sup>]<sup>tet</sup>[Fe<sup>2+</sup>, Fe<sup>3+</sup>]<sup>oct</sup>O<sub>4</sub>. [8] In a “normal” Co<sub>2</sub>MnO<sub>4</sub> spinel, the octahedral sites are occupied by Co<sup>3+</sup> ions and the tetrahedral sites by Mn<sup>2+</sup> ions. Conversely, in an inverse Co<sub>2</sub>MnO<sub>4</sub> spinel, like the structure identified in the experiments, half of the octahedral sites are occupied by Co<sup>3+</sup> ions and the other half by Mn<sup>3+</sup> ions, while the tetrahedral sites are all occupied by Co<sup>2+</sup> ions. Given the technical complexity in simulating chemical disorder/partial occupancies at the octahedral sites for the inverse spinel, [9] which would require sampling many different configurations and subsequently perform statistical averages, and the likeliness in obtaining very similar trends upon Ni doping for

both the normal and inverse spinel configurations, in this study we chose to model the normal spinel configuration.

The latter assertion was based on the reasonable assumption that the following energy relationship between the two spinel configurations holds:

$$E_{DFT}(inverse) - E_{DFT}(normal) \approx E_{bulk}(inverse) - E_{bulk}(normal)$$

Hence, one may conclude that:

$$E_{surf}(inverse) \approx E_{surf}(normal)$$

Thus, equivalent surface formation energy  $E_{surf}$  results were likely to be obtained whether considering the “inverse” or “normal” spinel configurations. This approach ensured that our DFT simulations remained computationally feasible while still providing meaningful insights into the surface properties of  $\text{Co}_2\text{MnO}_4$ .

The demetallization tendency and surface oxygen loss energy for the (400) surface were estimated by computing the vacancy formation energy of Co, Mn and O ions in the  $\text{Co}_2\text{MnO}_4$  and Ni-doped  $\text{Co}_2\text{MnO}_4$  systems. These results were obtained for the same slab configurations that were employed in the energy surface calculations.

### ***Rietveld refinement analysis***

The Rietveld refinements were conducted using the HighScore Plus software from PANalytical. The initial structural model for  $\text{Co}_2\text{MnO}_4$  was obtained from the Inorganic Crystallographic Structure Database (ICSD, 291115). The refinement process began by assuming a Co-to-Mn ratio of 2:1, based on our ICP-OES results.

Our XANES and EXAFS analyses indicated that Co primarily occupies the tetrahedral sites, while Ni, Co, and Mn share the octahedral sites within the  $\text{Co}_2\text{MnO}_4$  spinel structure. Initially, the refinement assumed that Ni substituted Mn at the octahedral sites. However, this assumption led to an increased R-factor, indicating that the model did not accurately fit the observed diffraction pattern.

The refinement was then adjusted to assume that Ni ions replaced Co ions at the octahedral sites. The iterative refinement began with a Ni concentration of 1% (Site occupancy at the octahedral site: Co = 0.49, Mn = 0.5, Ni = 0.01). The software automatically adjusted the occupancy of each element during the refinement process, and a decrease in the R-factor confirmed that this model provided a better fit with the experimental data.

The final Rietveld refinement results confirmed that Ni ions preferentially substitute Co ions at the octahedral sites in the  $\text{Co}_2\text{MnO}_4$  spinel structure. This conclusion is supported by the observed reduction in the R-factor, signifying a strong match between the calculated and observed diffraction patterns. A more detailed mathematical model for this substitution can be found in previous literature.

### **Membrane Electrode Assembly and PEM water electrolysis**

The Nafion 117 membrane was sequentially boiled in H<sub>2</sub>O<sub>2</sub>, deionized (DI) water, 1 M H<sub>2</sub>SO<sub>4</sub>, and DI water at 80°C for 1 hour each before hot-pressing the membrane electrode assembly (MEA). The active surface area of both the anode and cathode was 1 cm<sup>2</sup>. The cathode catalyst ink for the cathode was prepared by mixing 20% Pt/C with 5% Nafion 117 solution and ethanol, followed by ultrasonication for 1 hour before use. The catalyst-to-Nafion solution ratio was 3:1 (75 wt% catalyst, 25 wt% Nafion 117 solution). The ink was spray-coated onto a Ti fiber felt, with the catalyst loading controlled at 3 mg cm<sup>-2</sup>. The anode was prepared on Pt/Ti felt using the previously mentioned thermal decomposition method, with a catalyst loading of 4 mg cm<sup>-2</sup>.

The cathode, membrane, and anode were hot-pressed at 2 MPa for 3 minutes at 120 °C to form the MEA. The MEA was installed into a PEMWE cell with serpentine flow channels of 2 cm<sup>2</sup> area on both sides. At least three independent MEAs were tested for replication. The cell temperature was maintained at 80 °C, and DI water was fed exclusively to the anode side only, at a flow rate of 0.5 mL min<sup>-1</sup>.

## Figures

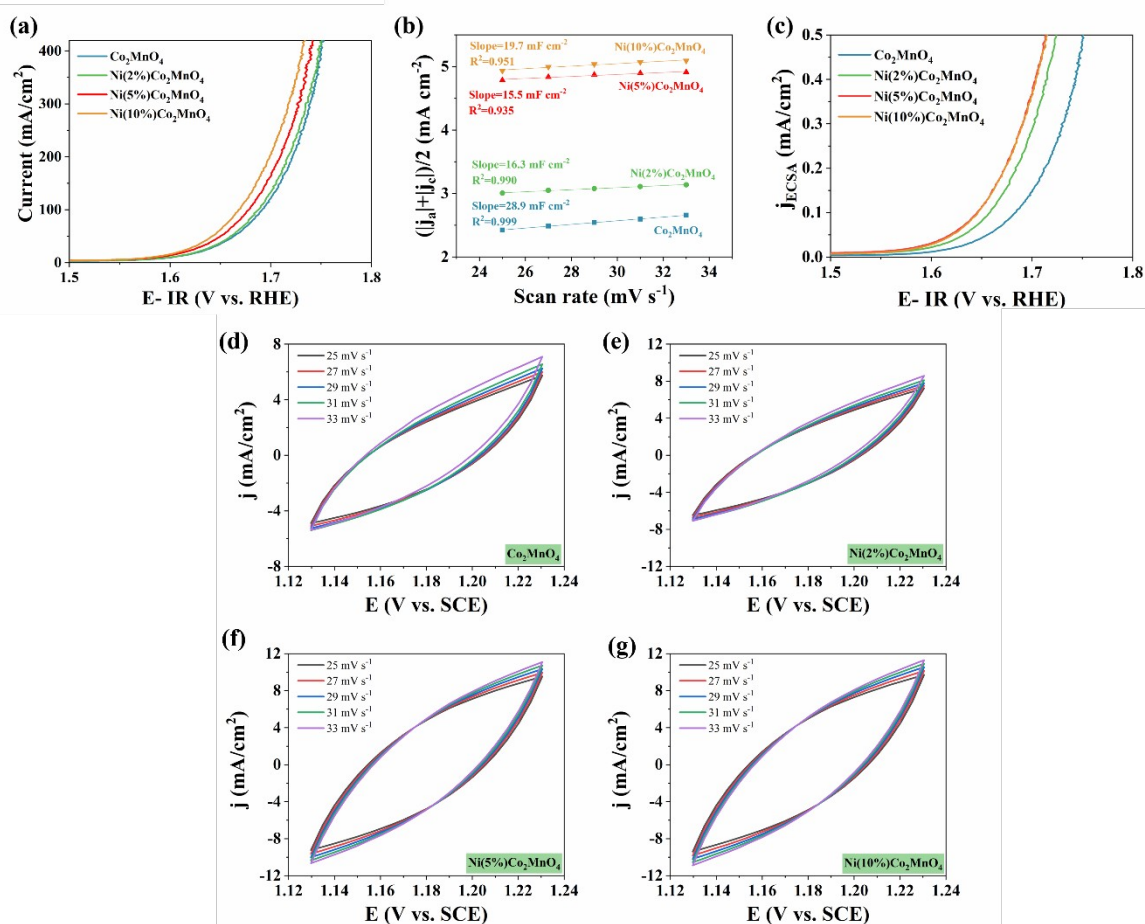


**Figure S1.** (a) Linear sweep voltammetry (LSV) curves. (b) Electrochemical double-layer capacitance ( $C_{dl}$ ) values ( $\text{Co}_2\text{MnO}_4$ :  $824 \text{ cm}^2$ ;  $\text{Ni}(2\%)\text{Co}_2\text{MnO}_4$ :  $465 \text{ cm}^2$ ;  $\text{Ni}(5\%)\text{Co}_2\text{MnO}_4$ :  $444 \text{ cm}^2$ ;  $\text{Ni}(10\%)\text{Co}_2\text{MnO}_4$ :  $561 \text{ cm}^2$ ). (c) LSV curves normalized by ECSA. The corresponded CV curves for (d)  $\text{Co}_2\text{MnO}_4$ , (e)  $\text{Ni}(2\%)\text{Co}_2\text{MnO}_4$ , (f)  $\text{Ni}(5\%)\text{Co}_2\text{MnO}_4$  and (g)  $\text{Ni}(10\%)\text{Co}_2\text{MnO}_4$ .

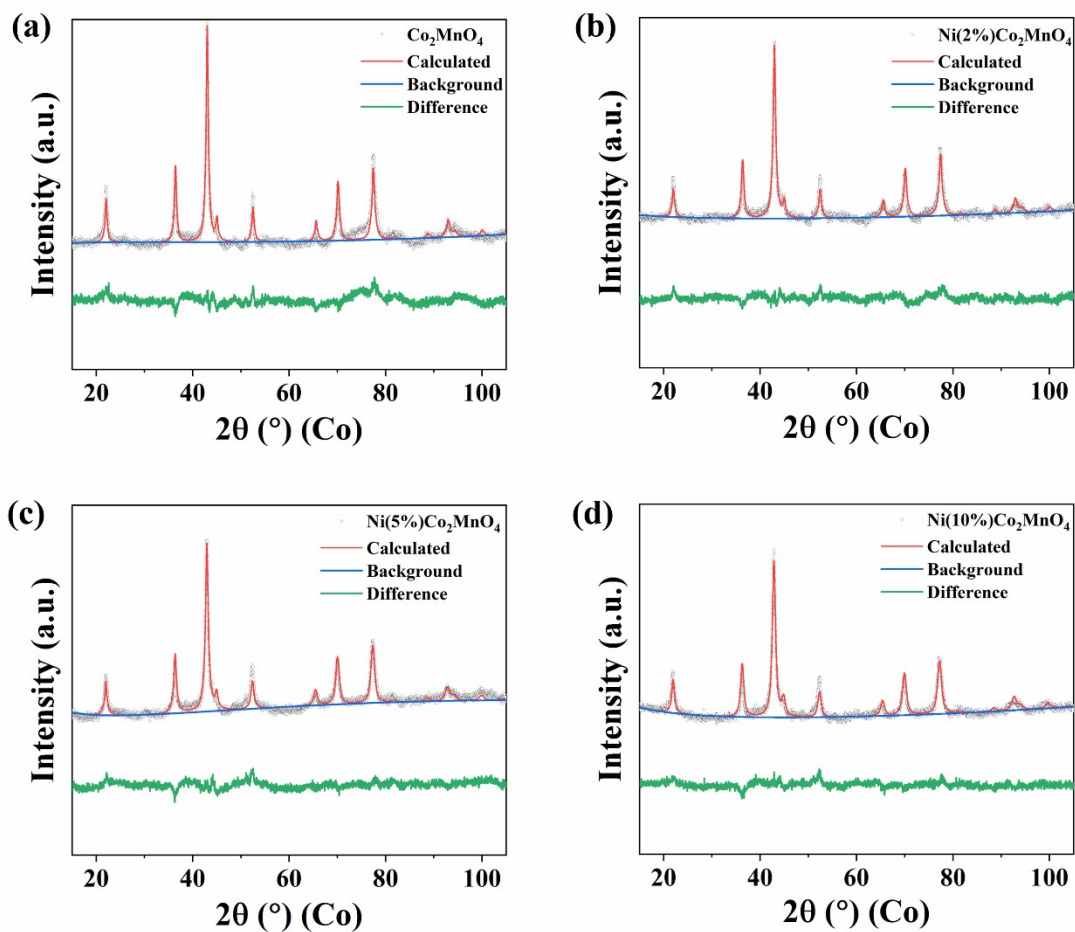


**Figure S2.** Rietveld refinement for the powder XRD pattern of (a)  $\text{Co}_2\text{MnO}_4$ , (b)  $\text{Ni}(2\%)\text{Co}_2\text{MnO}_4$ , (c)  $\text{Ni}(5\%)\text{Co}_2\text{MnO}_4$  and (d)  $\text{Ni}(10\%)\text{Co}_2\text{MnO}_4$ . The structural parameters derived from Rietveld refinement were given in Table S3-6.

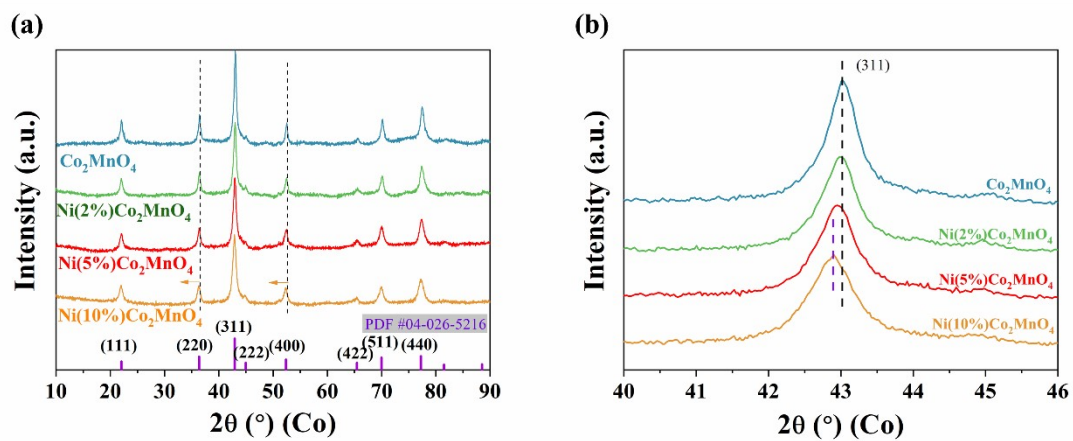


**Figure S3.** (a) XRD patterns of pristine  $\text{Co}_2\text{MnO}_4$  and Ni-doped  $\text{Co}_2\text{MnO}_4$ . (b) Enlarged XRD patterns of (311) plane of pristine  $\text{Co}_2\text{MnO}_4$  and different Ni-doped ratio of  $\text{Co}_2\text{MnO}_4$ .

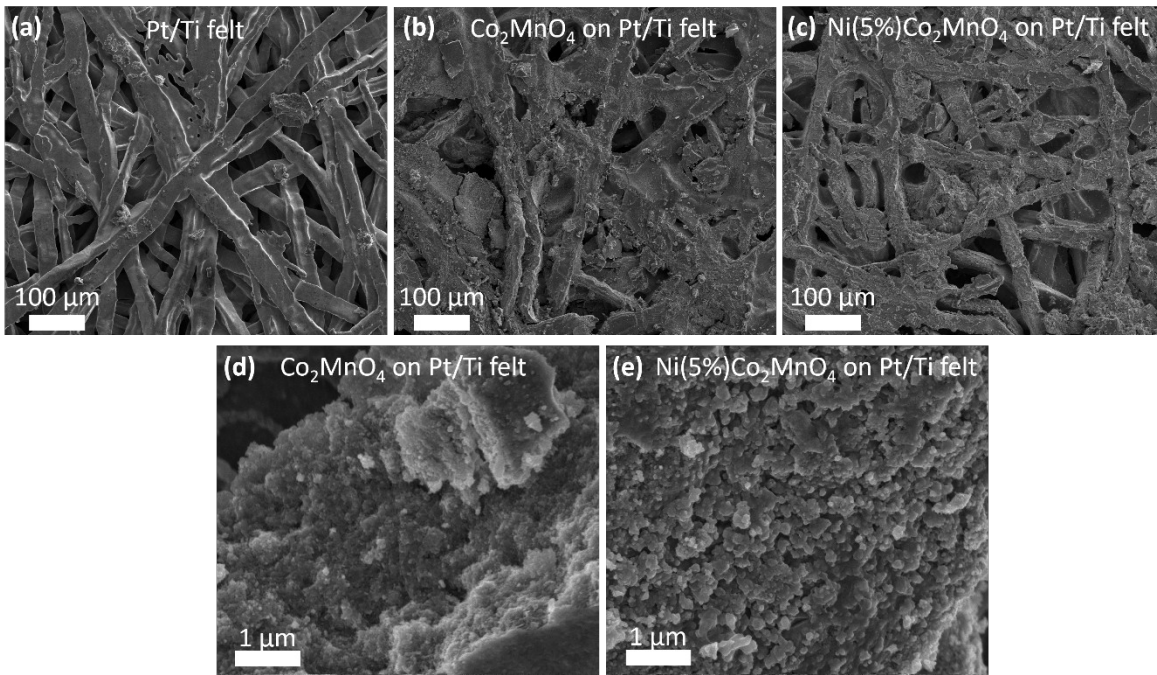


**Figure S4.** SEM images of (a) Pt/Ti fibre felt, (b)  $\text{Co}_2\text{MnO}_4$ , (c)  $\text{Ni}(5\%)\text{Co}_2\text{MnO}_4$ . High-resolution SEM images of (d)  $\text{Co}_2\text{MnO}_4$  and (e)  $\text{Ni}(5\%)\text{Co}_2\text{MnO}_4$ .

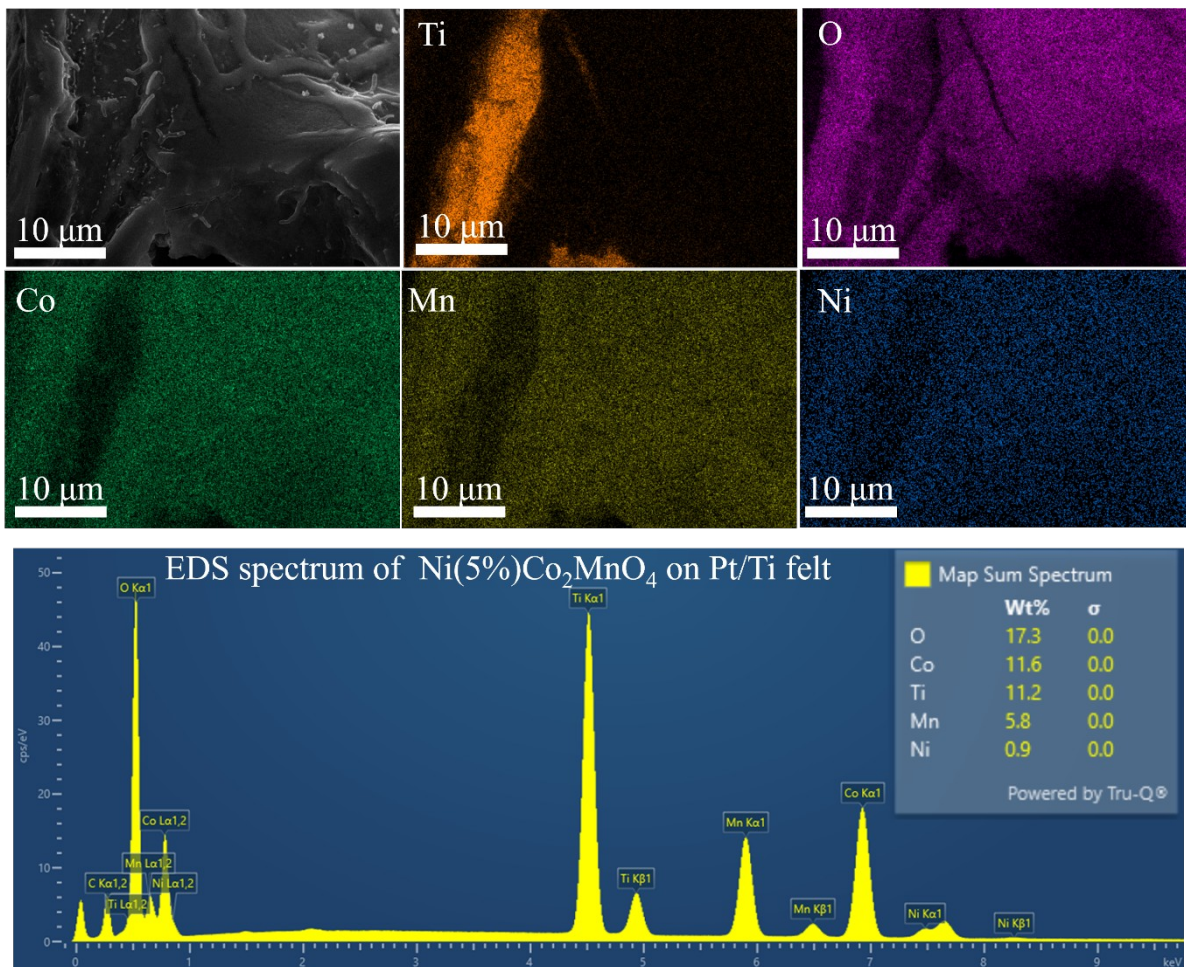


**Figure S5.** Elements mapping and the corresponding EDS spectrum for the selected area of Ni(5%)Co<sub>2</sub>MnO<sub>4</sub>.

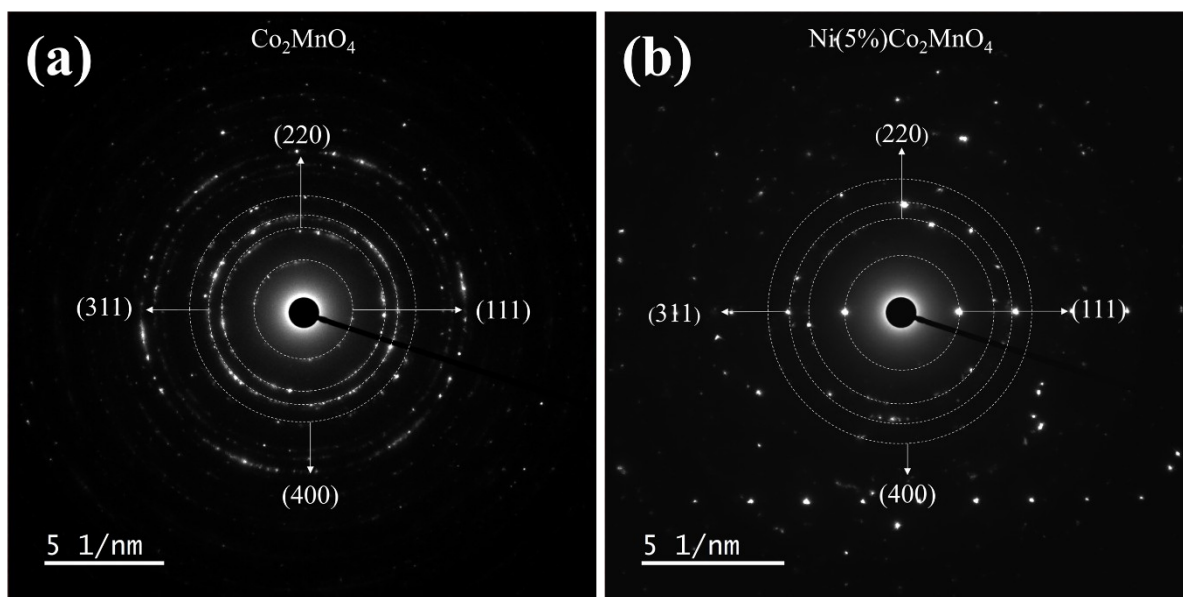


**Figure S6.** Selected area electron diffraction (SAED) patterns of (a) pristine  $\text{Co}_2\text{MnO}_4$  and (b)  $\text{Ni}(5\%)\text{Co}_2\text{MnO}_4$  powder.

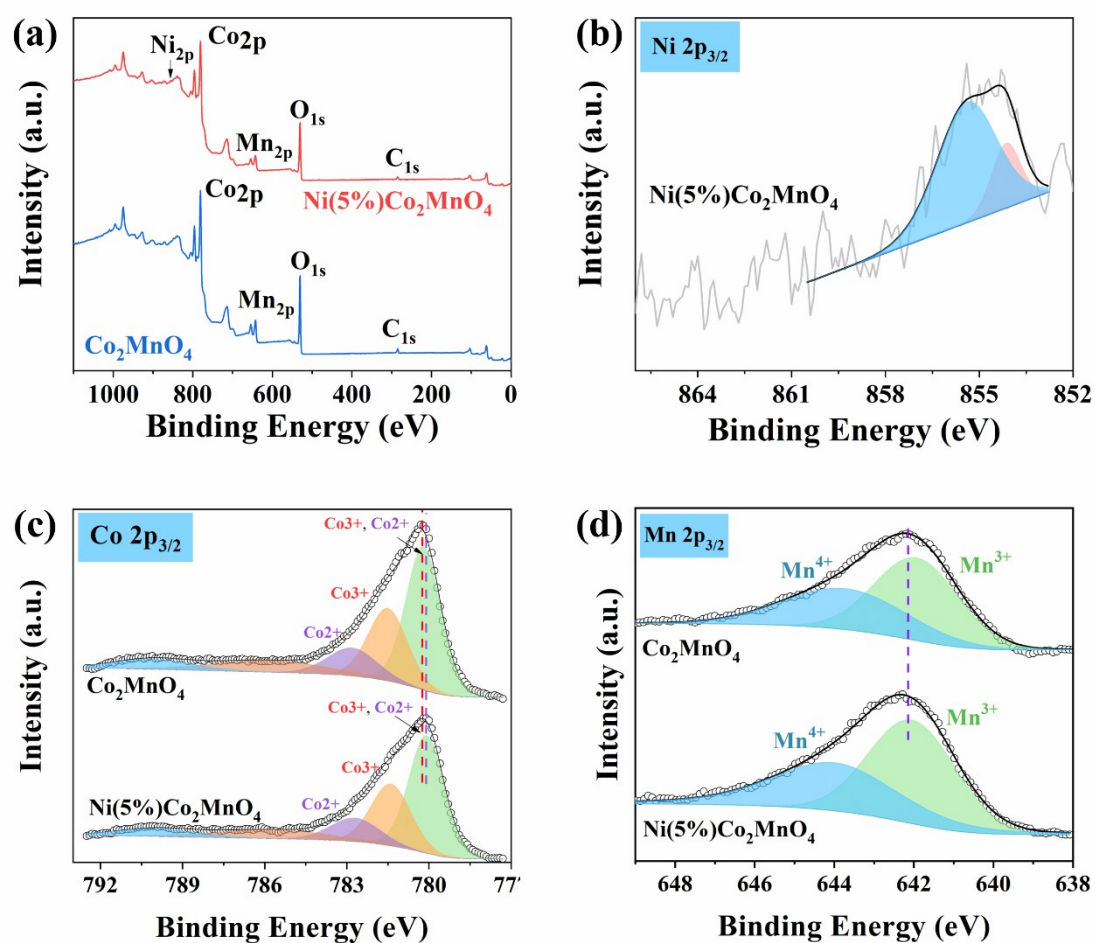


**Figure S7.** (a) XPS survey spectra of  $\text{Co}_2\text{MnO}_4$  powder and  $\text{Ni(5\%)\text{Co}_2\text{MnO}_4}$  powder. Deconvoluted XPS spectra of the (b)  $\text{Ni } 2p_{3/2}$  region, (c)  $\text{Co } 2p_{3/2}$  region and (d)  $\text{Mn } 2p_{3/2}$  region.

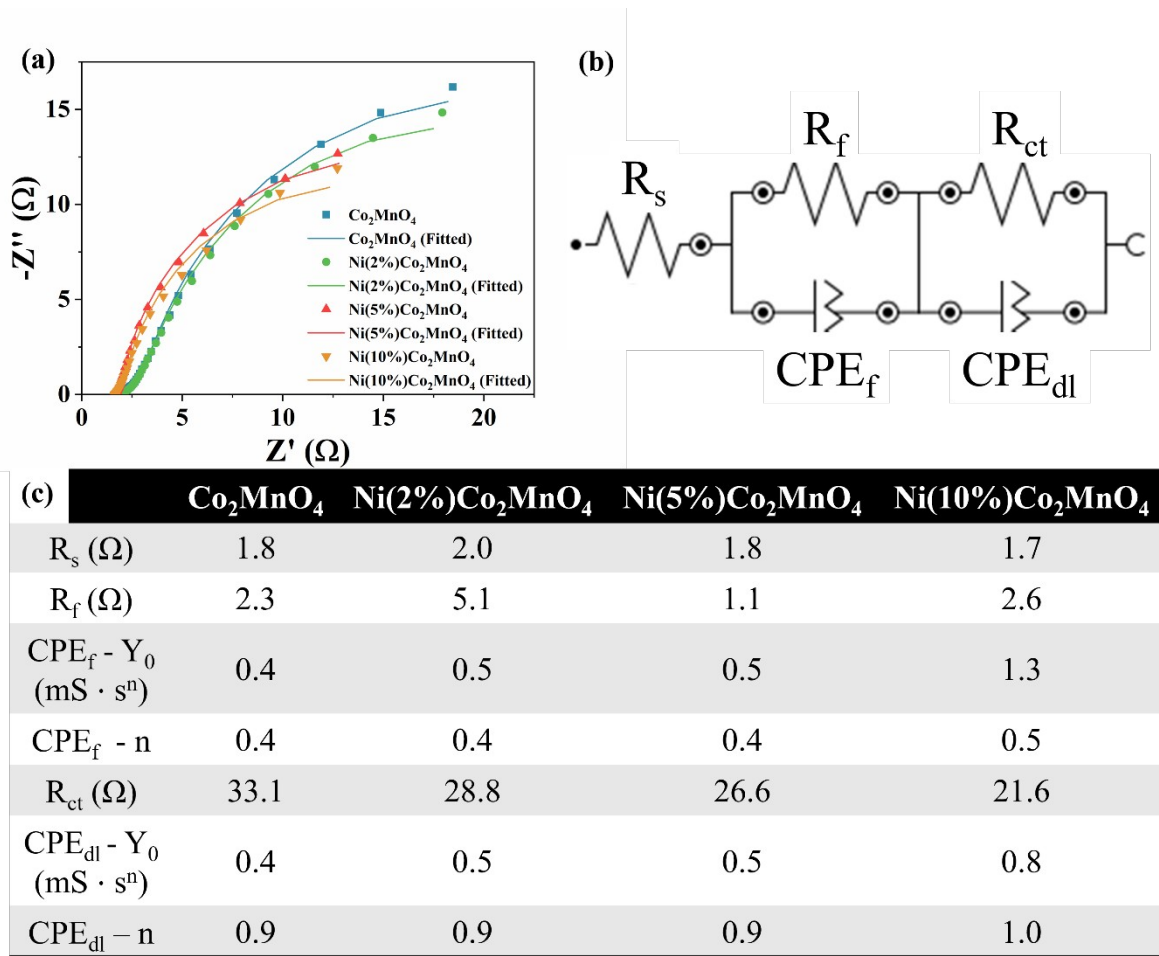


**Figure S8.** (a) Nyquist plot. The curves were fitted with the NOVA software using the equivalent circuit models shown in (b).<sup>[10]</sup> The solution resistance ( $R_s$ ), the film resistance ( $R_f$ ) and the charge transfer resistance ( $R_{ct}$ ). The constant phase element of film ( $\text{CPE}_f$ ) and constant phase element of double layer ( $\text{CPE}_{dl}$ ). (c) The corresponding fitting parameters.

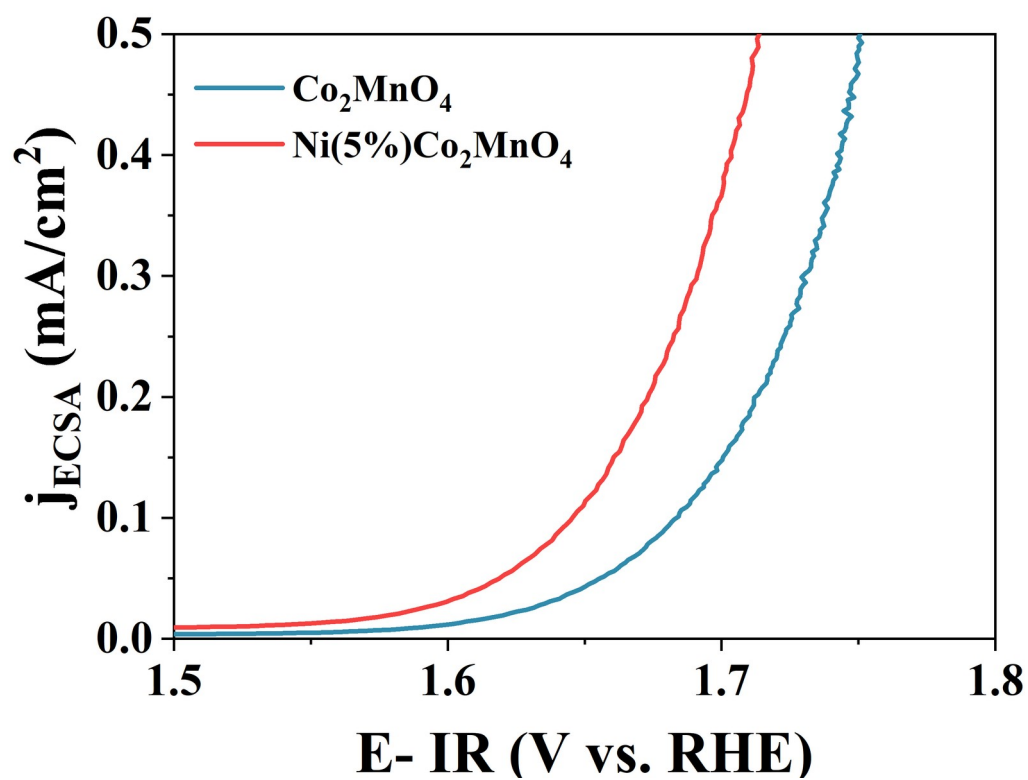


**Figure S9.** LSV curves of  $\text{Co}_2\text{MnO}_4$  and  $\text{Ni}(5\%)\text{Co}_2\text{MnO}_4$  normalized by ECSA.

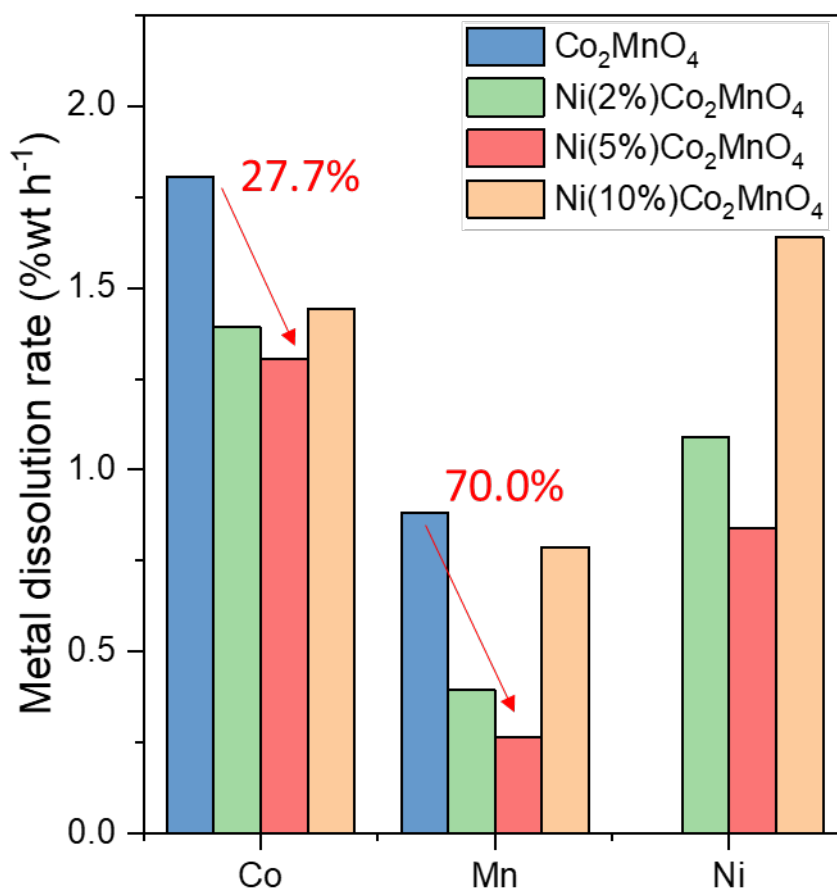


**Figure S10. Inductively Coupled Plasma Optical Emission Spectroscopy (ICP-OES).** Co, Mn and Ni dissolution rates of Co<sub>2</sub>MnO<sub>4</sub>, Ni(2%)Co<sub>2</sub>MnO<sub>4</sub>, Ni(5%)Co<sub>2</sub>MnO<sub>4</sub> and Ni(10%)Co<sub>2</sub>MnO<sub>4</sub>.

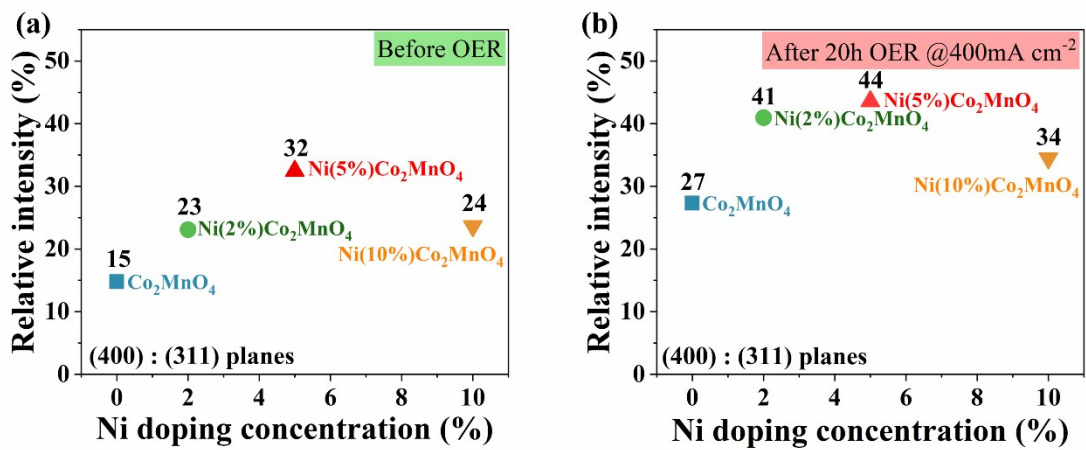


**Figure S11.** The relative intensity ratio of (400) to (311) planes (a) before OER reaction, (b) after 20h OER at 400 mA cm<sup>-2</sup>.

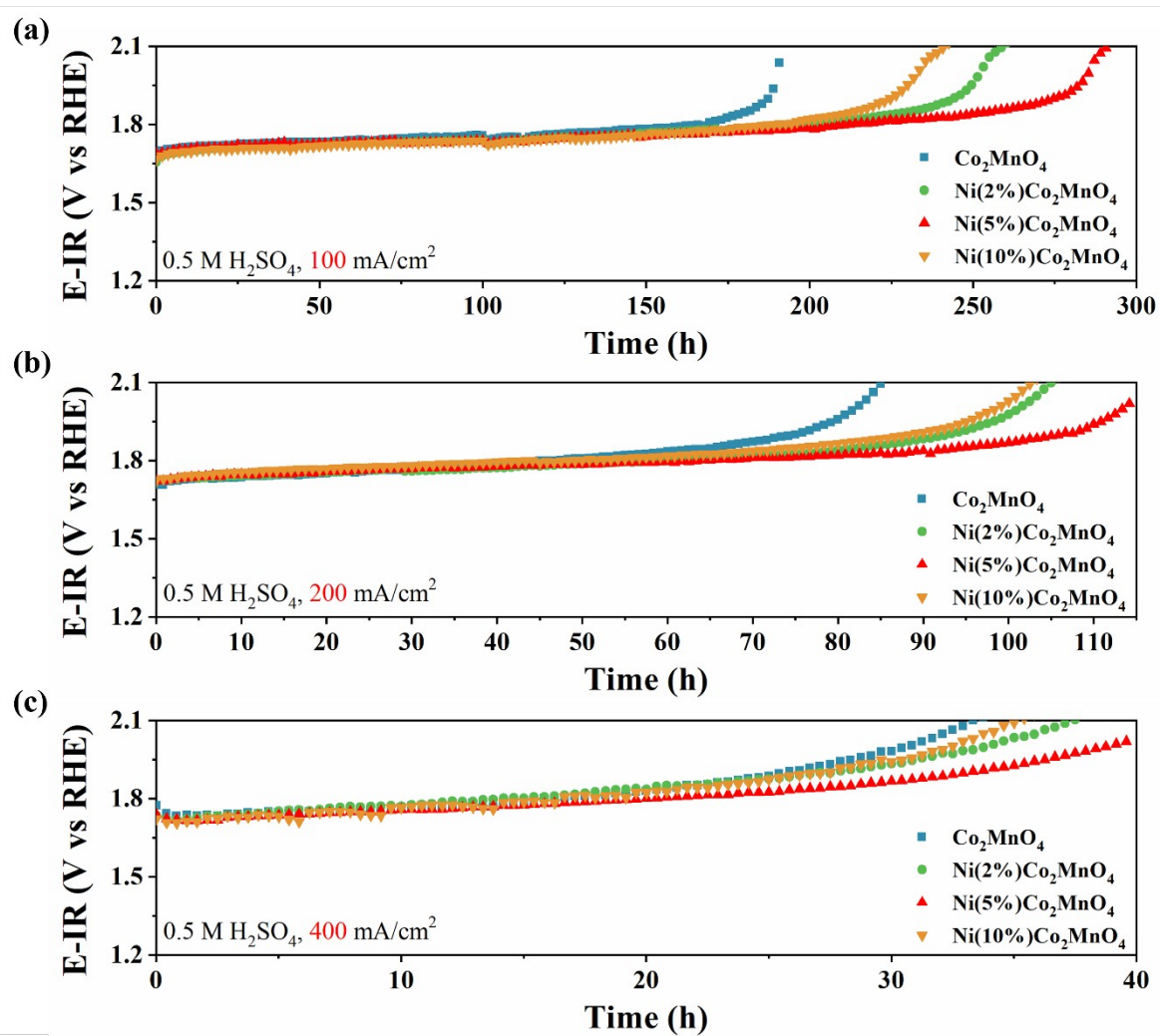


**Figure S12.** Stability evaluation at a current density of (a)  $100 \text{ mA cm}^{-2}$ , (b)  $200 \text{ mA cm}^{-2}$ , and (c)  $400 \text{ mA cm}^{-2}$  for  $\text{Co}_2\text{MnO}_4$  and different Ni-doped ratio of  $\text{Co}_2\text{MnO}_4$ .

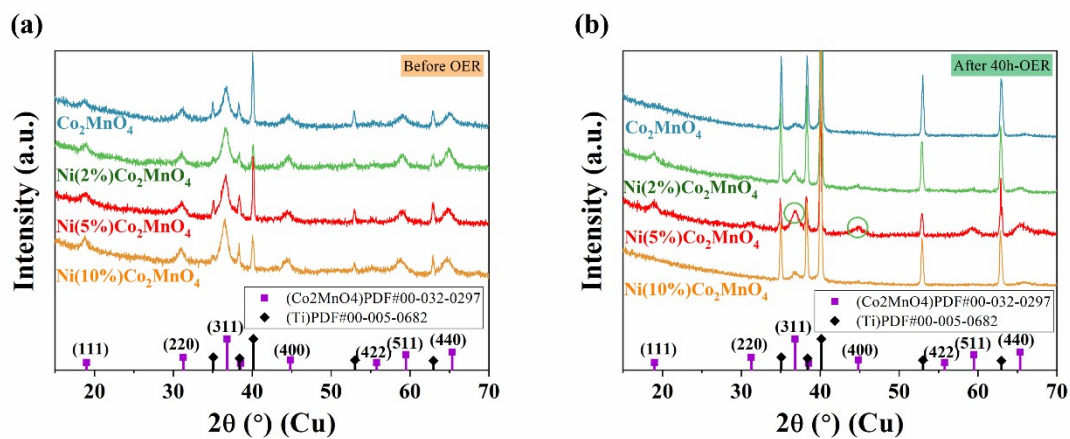


**Figure S13.** XRD pattern of  $\text{Co}_2\text{MnO}_4$  doped with different Ni ratios (0%, 2%, 5%, 10%) on the Pt/Ti felt: (a) before OER reaction and (b) after 40 hours OER reaction at  $400 \text{ mA cm}^{-2}$ .

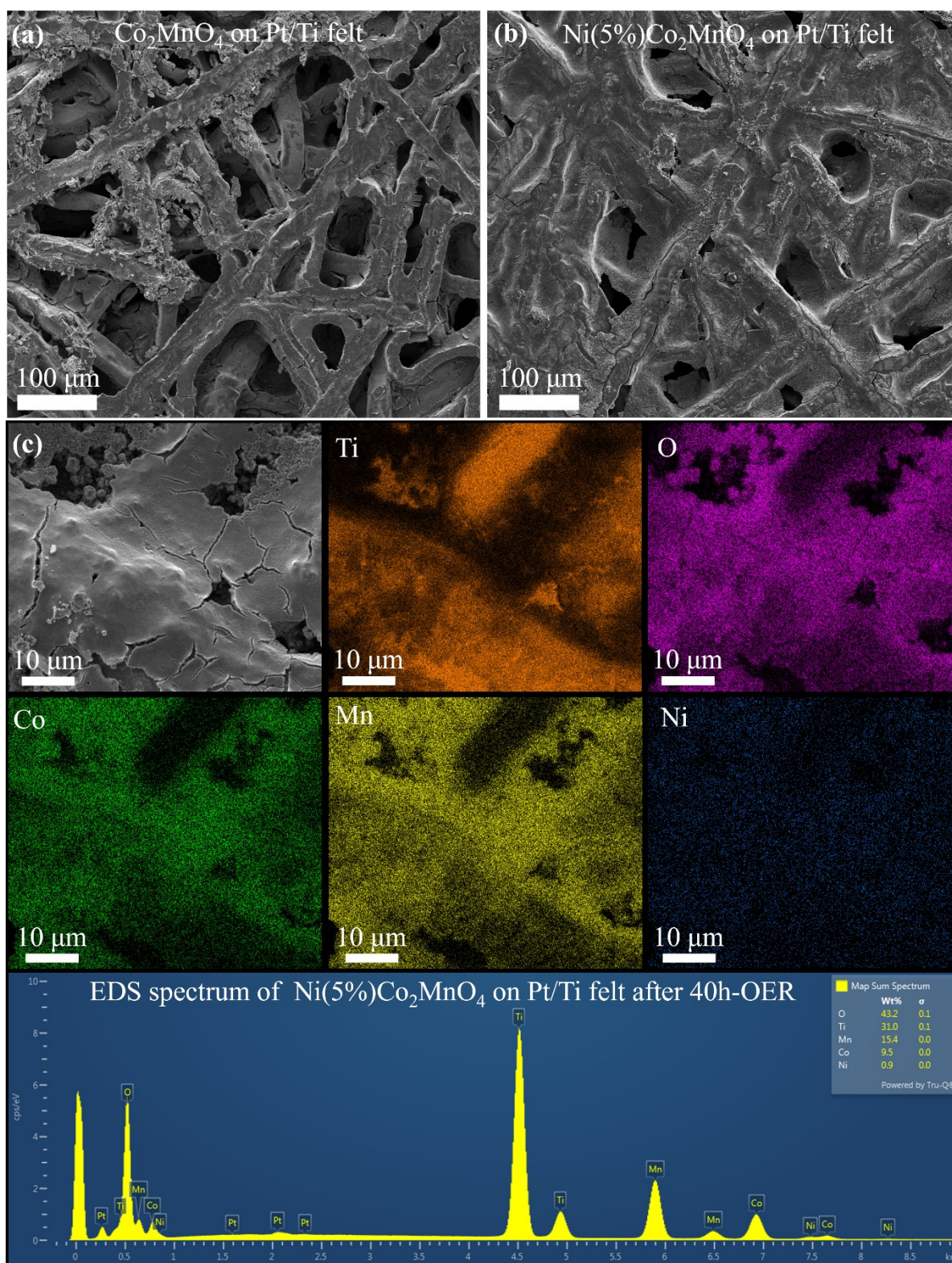


**Figure S14.** SEM images of (a)  $\text{Co}_2\text{MnO}_4$  and (b)  $\text{Ni}(5\%)\text{Co}_2\text{MnO}_4$ , after 40 hours of OER reactions. (c) The elemental mapping and (d) the corresponding EDS spectrum for the selected area of  $\text{Ni}(5\%)\text{Co}_2\text{MnO}_4$  after 40 hours of OER reactions.

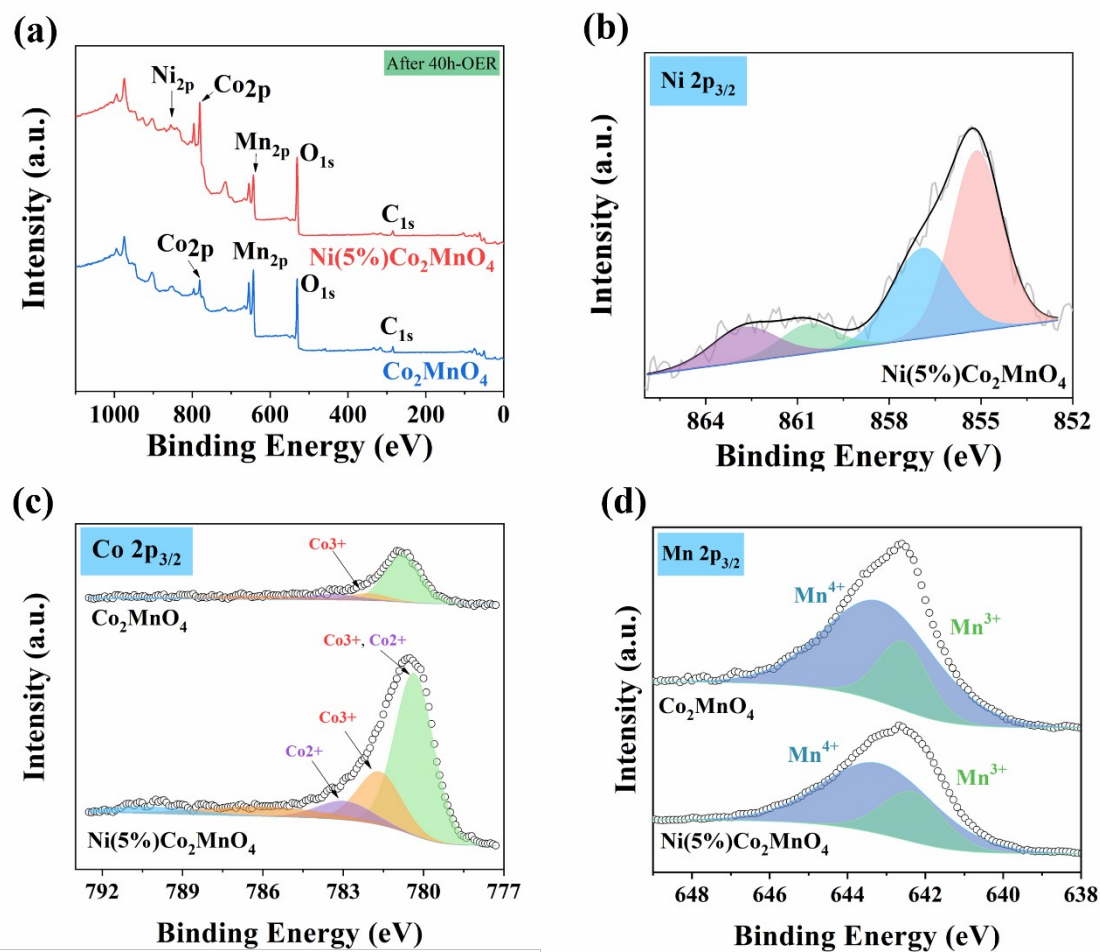


**Figure S15.** (a) XPS survey spectra of  $\text{Co}_2\text{MnO}_4$  and  $\text{Ni}(5\%)\text{Co}_2\text{MnO}_4$  after 40 hours OER reactions at  $400 \text{ mA cm}^{-2}$ . Deconvoluted XPS spectra of the (b)  $\text{Ni } 2p_{3/2}$  region, (c)  $\text{Co } 2p_{3/2}$  region and (d)  $\text{Mn } 2p_{3/2}$  region.

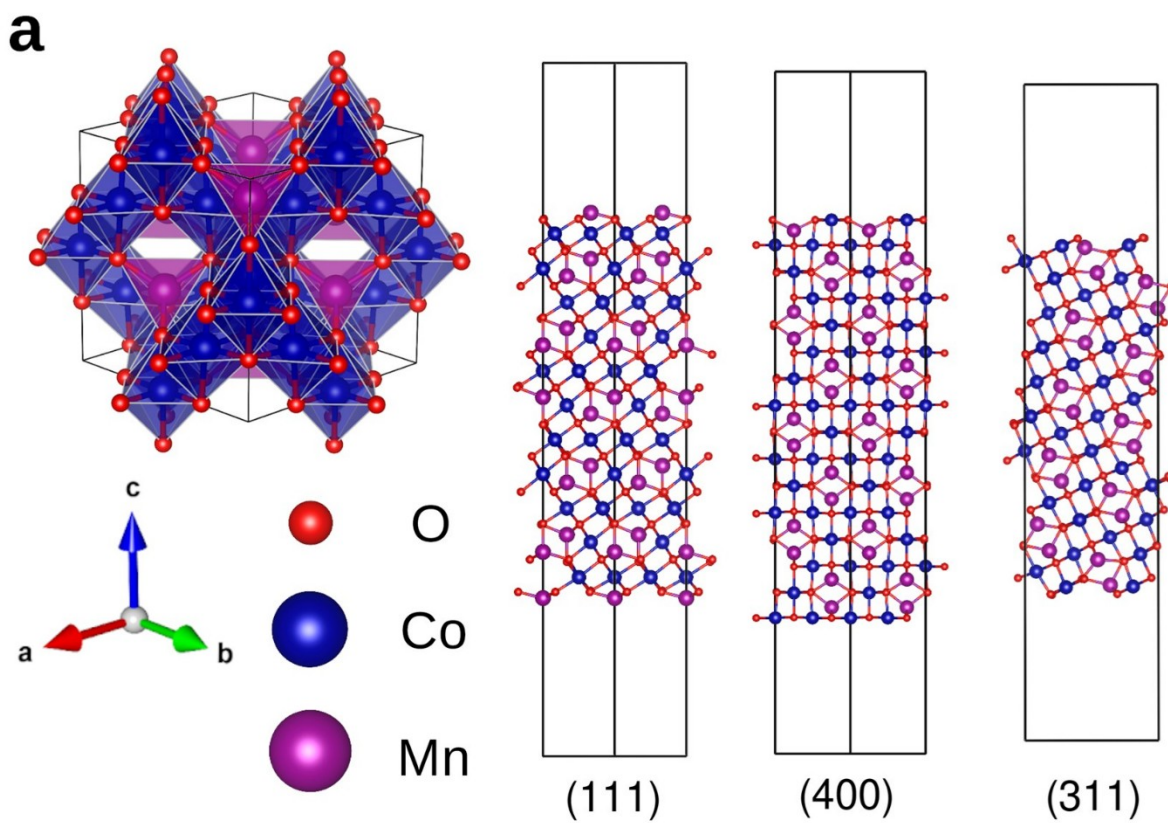


**Figure S16.** DFT models of  $\text{Co}_2\text{MnO}_4$  and corresponding (111), (311) and (400) facets. The Co, Mn, and O ions are represented with blue, purple and red spheres, respectively.

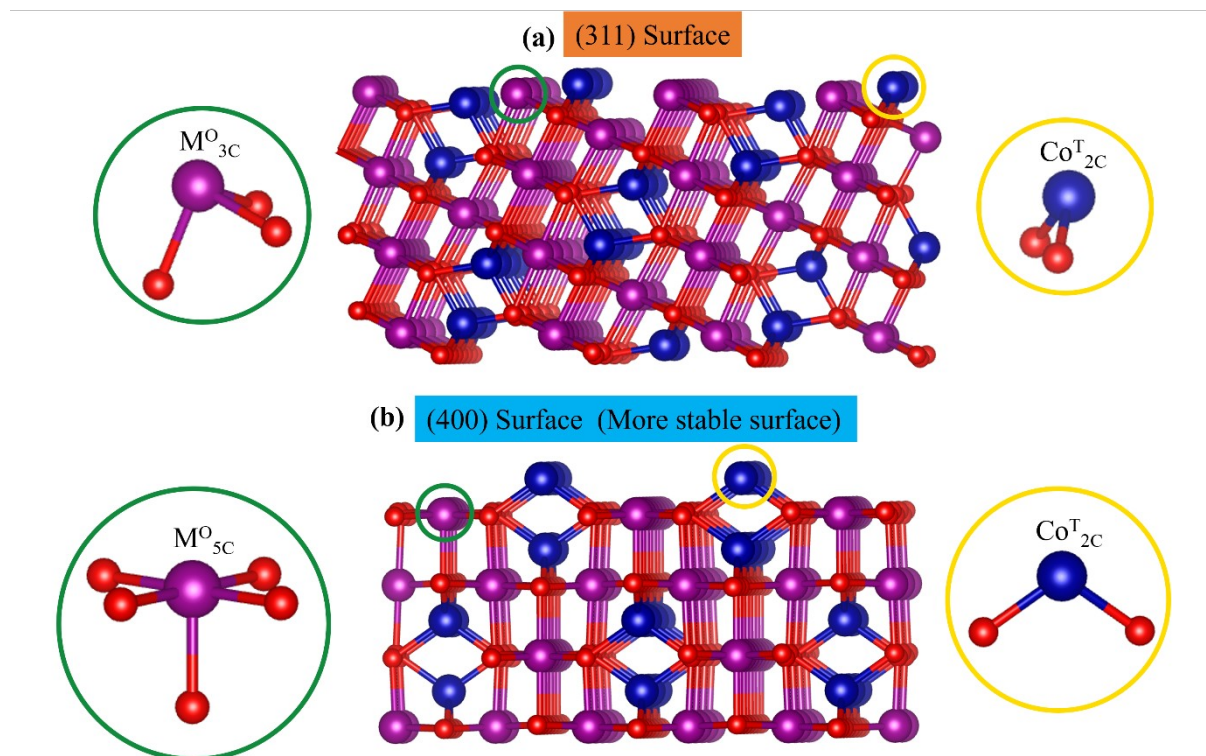


**Figure S17.** Illustration of (a) (311), and (b) (400) surface. These structure models are generated by VESTA software<sup>[11]</sup>. The blue sphere at tetrahedral site representing Co ions and purple ions representing metal ions (M = Co, Mn or Ni) at octahedral sites. The 5-fold coordinated metal ion at octahedral sites on (400) surface is believed to be more stable than the 3-fold coordinated metal ion at tetrahedral sites.<sup>[12]</sup>

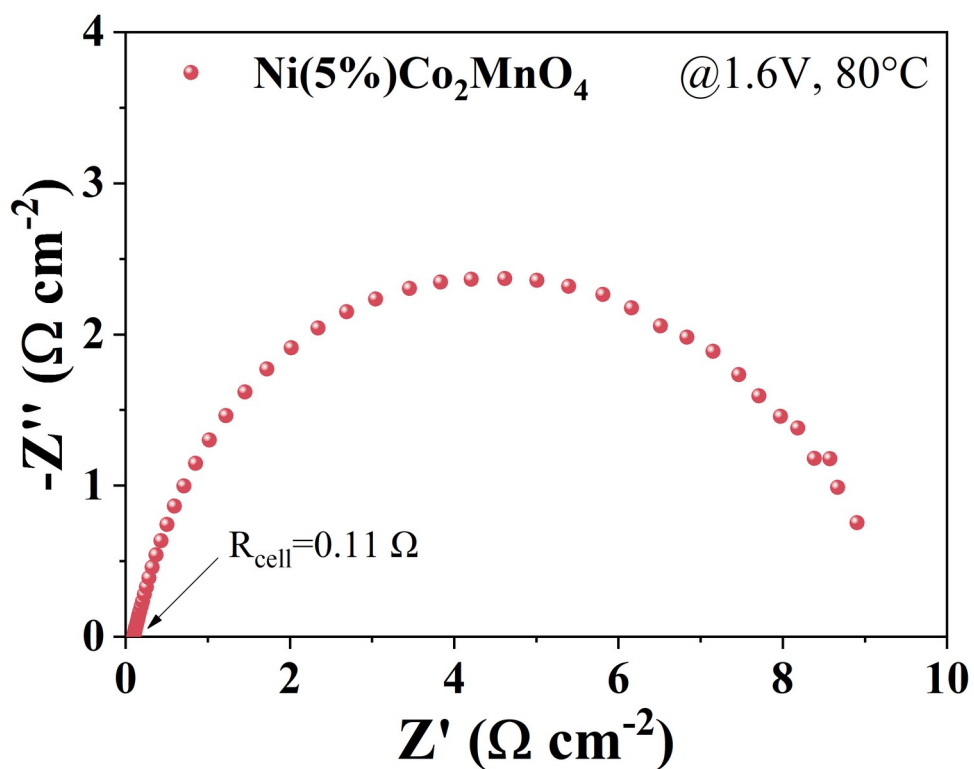


**Figure S18.** Nyquist plot of the PEMWE cell with an anode catalyst of Ni(5%)Co<sub>2</sub>MnO<sub>4</sub> and a cathode catalyst of Pt/C. The cell resistance ( $R_{\text{cell}}$ ) was determined through EIS conducted from 500 kHz to 0.1 Hz with a 5-mV amplitude.

**Table S1:** The inductively coupled plasma optical emission spectrometry (ICP-OES) results for  $\text{Co}_2\text{MnO}_4$  and Ni-doped  $\text{Co}_2\text{MnO}_4$

Sample	Co[%wt]	Mn[%wt]	Ni[%wt]	Co : Mn	Ni : (Co+Mn)
$\text{Co}_2\text{MnO}_4$	49.4	24.6	-	2.01	-
Ni(2%) $\text{Co}_2\text{MnO}_4$	47.9	23.8	1.4	2.01	2.0%
Ni(5%) $\text{Co}_2\text{MnO}_4$	47.2	22.9	3.5	2.06	5.0%
Ni(10%) $\text{Co}_2\text{MnO}_4$	44.9	22.1	6.7	2.03	9.9%

**Table S2:** Lattice constant of  $\text{Co}_2\text{MnO}_4$  and Ni-doped  $\text{Co}_2\text{MnO}_4$

Ni doping concentration	Lattice constant (Å)
0%	$8.090 \pm 0.003$
2%	$8.091 \pm 0.003$
5%	$8.098 \pm 0.003$
10%	$8.108 \pm 0.003$

**Table S3** Structural parameters of Co<sub>2</sub>MnO<sub>4</sub> derived from Rietveld refinement.

No.	Atom	Wyck.	x	y	z	sof	B <sub>iso</sub>
1	Co1	8b (Tetrahedral)	0.375	0.375	0.375	1.00 0	0.5
2	Co2	16c (Octahedral)	0.000	0.000	0.000	0.50 8	0.5
3	Mn1	16c (Octahedral)	0.000	0.000	0.000	0.49 2	0.5
4	O1	32e	0.237	0.237	0.237	1.00 0	0.5

Cubic crystal system; *Fd-3m* space group (space group number 227); Lattice parameters:  $a = 8.0896$  Å; Volume =  $529.4$  Å<sup>3</sup>;  $R_{exp}$  (Expected profile R-value) = 1.38%,  $R_{wp}$  (Weighted Profile R-value) = 2.29%, GOF (goodness of fit,  $\chi^2$ ) = 1.66; 14 refined variables; sof, occupancy; B<sub>iso</sub>, isotropic atomic displacement parameters. The structure is available on The Cambridge Crystallographic Data Centre (<https://www.ccdc.cam.ac.uk/>), deposition number CSD 2356887.

**Table S4** Structural parameters of Ni(2%)Co<sub>2</sub>MnO<sub>4</sub> derived from Rietveld refinement.

No.	Atom	Wyck.	x	y	z	sof	B <sub>iso</sub>
1	Co1	8b (Tetrahedral)	0.375	0.375	0.375	1.00 0	0.5
2	Co2	16c (Octahedral)	0.000	0.000	0.000	0.47 2	0.5
3	Mn1	16c (Octahedral)	0.000	0.000	0.000	0.47 6	0.5
4	O1	32e	0.240	0.240	0.240	1.00 0	0.5
5	Ni1	16c (Octahedral)	0.000	0.000	0.000	0.05 4	0.5

Cubic crystal system; *Fd-3m* space group (space group number 227); Lattice parameters:  $a = 8.0907$  Å; Volume =  $529.6$  Å<sup>3</sup>;  $R_{exp} = 1.49\%$ ,  $R_{wp} = 1.95\%$ , GOF = 1.31; 14 refined variables; sof, occupancy; B<sub>iso</sub>, isotropic atomic displacement parameters. The structure is available on The Cambridge Crystallographic Data Centre (<https://www.ccdc.cam.ac.uk/>), deposition number CSD 2356888.

**Table S5** Structural parameters of Ni(5%)Co<sub>2</sub>MnO<sub>4</sub> derived from Rietveld refinement.

No.	Atom	Wyck.	x	y	z	sof	B <sub>iso</sub>
1	Co1	8b (Tetrahedral)	0.375	0.375	0.375	1.00 0	0.5
2	Co2	16c (Octahedral)	0.000	0.000	0.000	0.44 1	0.5
3	Mn1	16c (Octahedral)	0.000	0.000	0.000	0.46 0	0.5
4	O1	32e	0.237	0.237	0.237	1.00 0	0.5
5	Ni1	16c (Octahedral)	0.000	0.000	0.000	0.09 9	0.5

Cubic crystal system; *Fd-3m* space group (space group number 227); Lattice parameters:  $a = 8.0982$  Å; Volume = 531.1 Å<sup>3</sup>;  $R_{exp} = 1.51\%$ ,  $R_{wp} = 2.17\%$ ,  $GOF = 1.44$ ; 14 refined variables; sof, occupancy;  $B_{iso}$ , isotropic atomic displacement parameters. The structure is available on The Cambridge Crystallographic Data Centre (<https://www.ccdc.cam.ac.uk/>), deposition number CSD 2356889.

**Table S6** Structural parameters of Ni(10%)Co<sub>2</sub>MnO<sub>4</sub> derived from Rietveld refinement.

No.	Atom	Wyck.	x	y	z	sof	B <sub>iso</sub>
1	Co1	8b (Tetrahedral)	0.375	0.375	0.375	1.00 0	0.5
2	Co2	16c (Octahedral)	0.000	0.000	0.000	0.38 2	0.5
3	Mn1	16c (Octahedral)	0.000	0.000	0.000	0.40 8	0.5
4	O1	32e	0.240	0.240	0.240	1.00 0	0.5
5	Ni1	16c (Octahedral)	0.000	0.000	0.000	0.21 1	0.5

Cubic crystal system; *Fd-3m* space group (space group number 227); Lattice parameters:  $a = 8.1089$  Å; Volume = 533.1 Å<sup>3</sup>;  $R_{exp} = 1.54\%$ ,  $R_{wp} = 1.93\%$ ,  $GOF = 1.25$ ; 14 refined variables; sof, occupancy;  $B_{iso}$ , isotropic atomic displacement parameters. The structure is available on The Cambridge Crystallographic Data Centre (<https://www.ccdc.cam.ac.uk/>), deposition number CSD 2356886.

**Table S7:** Fitting parameters of Ni 2p<sub>3/2</sub> for Ni(5%)Co<sub>2</sub>MnO<sub>4</sub> before OER reaction

<b>Ni 2P<sub>3/2</sub></b>	<b>Peak 1 (eV)</b>	<b>Area (%)</b>	<b>Peak 1 FWHM (eV)</b>	<b>Peak 2 (eV)</b>	<b>Area (%)</b>	<b>Peak 2 FWHM (eV)</b>
Ni(5%)Co <sub>2</sub> MnO <sub>4</sub>	854.2	17.5	1.02	855.4	82.5	2.38

**Table S8:** Absorption band edge energy of Ni k-edge

<b>Sample</b>	<b>Absorption edge (eV)</b>
Ni	8333.00
NiO	8342.96
Ni(5%)Co <sub>2</sub> MnO <sub>4</sub>	8344.33

**Table S9:** Fitting parameters of Co 2p<sub>3/2</sub> for pristine Co<sub>2</sub>MnO<sub>4</sub> and Ni(5%)Co<sub>2</sub>MnO<sub>4</sub> before OER reaction

Co 2p <sub>3/2</sub>	Peak 1	Area	Peak 1	Peak 2	Area	Peak 2	Peak 3	Area	Peak 3
	(eV)	(%)	FWH M (eV)	(eV)	(%)	FWH M (eV)	(eV)	(%)	FWH M (eV)
Co <sub>2</sub> MnO <sub>4</sub>	780.2	44.2	1.56	781.5	25.1	1.75	782.8	12.1	2.19
	Peak 4	Area	Peak 4	Peak 5	Area	Peak 5			
	(eV)	(%)	FWH M (eV)	(eV)	(%)	FWH M (eV)			
	785.8	11.4	4.82	790.1	7.2	3.55			
Co 2p <sub>3/2</sub>	Peak 1	Area	Peak 1	Peak 2	Area	Peak 2	Peak 3	Area	Peak 3
	(eV)	(%)	FWH M (eV)	(eV)	(%)	FWH M (eV)	(eV)	(%)	FWH M (eV)
Ni(5%)Co <sub>2</sub> MnO <sub>4</sub>	780.1	44.3	1.57	781.4	26.1	1.77	782.7	12.6	2.21
	Peak 4	Area	Peak 4	Peak 5	Area	Peak 5			
	(eV)	(%)	FWH M (eV)	(eV)	(%)	FWH M (eV)			
	785.7	10.3	4.88	790.0	6.7	3.59			

**Table S10:** Absorption band edge energy of Co k-edge

Sample	Absorption edge (eV)
CoO	7714.50
Co <sub>3</sub> O <sub>4</sub>	7717.29
Ni(5%)Co <sub>2</sub> MnO <sub>4</sub>	7718.24
Co <sub>2</sub> MnO <sub>4</sub>	7718.49
Co <sub>2</sub> O <sub>3</sub>	7720.45

**Table S11:** Fitting parameters of Mn 2p<sub>3/2</sub> for pristine Co<sub>2</sub>MnO<sub>4</sub> and Ni(5%)Co<sub>2</sub>MnO<sub>4</sub> before OER reaction

<b>Mn 2P<sub>3/2</sub></b>	<b>Peak 1 (eV)</b>	<b>Area (%)</b>	<b>Peak 1 FWHM (eV)</b>	<b>Peak 2 (eV)</b>	<b>Area (%)</b>	<b>Peak 2 FWHM (eV)</b>
Co <sub>2</sub> MnO <sub>4</sub>	642.0	61.2	2.43	643.8	38.8	3.37
Ni(5%)Co <sub>2</sub> MnO <sub>4</sub>	642.0	65.3	2.57	643.9	34.7	3.37

**Table S12:** Absorption band edge energy of Mn k-edge

<b>Sample</b>	<b>Absorption edge (eV)</b>
MnO	6543.78
Co <sub>2</sub> MnO <sub>4</sub>	6550.75
Ni(5%)Co <sub>2</sub> MnO <sub>4</sub>	6550.77
MnO <sub>2</sub>	6553.58

**Table S13:** The activity and stability for non-noble metal-based oxide catalysts for OER in strong acidic electrolytes ( $\geq 0.5$  M  $\text{H}_2\text{SO}_4$ ).

Catalyst	$\text{H}_2\text{SO}_4$	Scan rate ( $\text{mV s}^{-1}$ )	$\eta_{10}$ ( $\text{mA cm}^{-2}$ )	Stability @ 10 mA $\text{cm}^{-2}$ (hours)	Stability@ 100 mA $\text{cm}^{-2}$ (hours)	Loading ( $\text{mg cm}^{-2}$ )	Year/ Ref.
Ni(5%) $\text{Co}_2\text{MnO}_4$	0.5 M	5	356	-	285	10	This work
$\text{Co}_2\text{MnO}_4$	0.5 M	5	371	-	190	10	This work
$\text{V}_o\text{-Co}_3\text{O}_4$ HNCs	0.5 M	5	295	100 130 <sup>a</sup>	20	1	2024 <sup>[13]</sup>
$\text{Co}_{3-x}\text{Ba}_x\text{O}_4$	0.5 M	5	278	110	-	1.6	2023 <sup>[14]</sup>
$\text{Co}_3\text{O}_4@\text{C}$	1 M	1	356	43	2	20	2022 <sup>[15]</sup>
$\text{C}_3\text{O}_4/\text{CeO}_2$	0.5 M	5	423	50	-	-	2021 <sup>[16]</sup>
$\text{Co}_{0.05}\text{Fe}_{0.95}\text{O}_y$	0.5 M	10	650	50	-	1	2019 <sup>[17]</sup>
c- $\text{Fe}_2\text{O}_3$	0.5 M	10	650	24	-	1	2018 <sup>[18]</sup>
$\text{Ni}_{0.5}\text{Mn}_{0.5}\text{Sb}_{1.7}\text{O}_y$	1 M	10	672	168	-	~0.18	2017 <sup>[19]</sup>
$\text{Co}_3\text{O}_4/\text{FTO}$	0.5 M	2	570	12	-	0.182	2017 <sup>[20]</sup>
$\text{Co}_3\text{O}_4@\text{C}$	0.5 M	5	370	-	86.8	12.6	2016 <sup>[21]</sup>

<sup>a</sup>: (@20mA  $\text{cm}^{-2}$ )

**Table S14:** DFT calculations – Surface formation Energy

	Pristine Co <sub>2</sub> MnO <sub>4</sub>	After (5%) of Ni doping	<b>Difference in surface formation energy</b>
<b>Facets</b>	$E_{surf}$ (J m <sup>-2</sup> )	$E_{surf}$ (J m <sup>-2</sup> )	$\Delta E_{surf}$
(111)	2.47	2.58	4.7%
(400)	2.37	2.21	-6.6%
(311)	3.91	3.19	-18.6%

**Table S15:** DFT calculations – Demetallization energy

		Pristine Co <sub>2</sub> MnO <sub>4</sub>	After (5%) of Ni doping	Difference in demetallization energy
<b>Metal ions</b>	<b>Facet</b>	<b>Demetallization energy <math>E_{pristine}</math> (eV)</b>	<b>Demetallization energy <math>E_{doped}</math> (eV)</b>	$\Delta E = (E_{doped} - E_{pristine}) / E_{pristine}$
Co	(111)	0.125	0.375	200.0%
Mn		0.175	0.295	68.6%
Co	(311)	0.551	0.851	54.4%
Mn		1.258	1.924	52.9%
Co	(400)	0.631	0.664	5.2%
Mn		0.121	0.162	33.9%

**Table S16:** DFT calculations – The ( $E_d - E_f$ ) values of **Co** ions

Co ions	Pristine Co <sub>2</sub> MnO <sub>4</sub>	After (5%) of Ni doping	<b>Difference in (<math>E_d - E_f</math>)</b>
<b>Facets</b>	$E_d - E_f$ (eV)	$E_d - E_f$ (eV)	$\Delta (E_d - E_f)$
(111)	1.951	1.937	-0.7%
(400)	1.855	1.910	3.0%
(311)	1.906	1.791	-6.0%

**Table S17:** DFT calculations – The ( $E_d - E_f$ ) values of **Mn** ions

Mn ions	Pristine Co <sub>2</sub> MnO <sub>4</sub>	After (5%) of Ni doping	<b>Difference in (<math>E_d - E_f</math>)</b>
<b>Facets</b>	$E_d - E_f$ (eV)	$E_d - E_f$ (eV)	$\Delta (E_d - E_f)$
(111)	1.121	0.793	-29.3%
(400)	1.928	1.184	-38.6%
(311)	1.163	0.830	-28.6%



## Reference

- [1] C. C. L. McCrory, S. Jung, I. M. Ferrer, S. M. Chatman, J. C. Peters, T. F. Jaramillo, *J Am Chem Soc* **2015**, 137, 4347.
- [2] C. Cazorla, O. Diéguez, J. Íñiguez, *Sci Adv* **2017**, 3, e1700288.
- [3] J. P. Perdew, A. Ruzsinszky, G. I. Csonka, O. A. Vydrov, G. E. Scuseria, L. A. Constantin, X. Zhou, K. Burke, *Phys Rev Lett* **2008**, 100, 136406.
- [4] G. Kresse, J. Furthmüller, *Physical Review B* **1996**, 54, 11169.
- [5] P. E. Blöchl, *Physical Review B* **1994**, 50, 17953.
- [6] a) C. Menéndez, C. Cazorla, *Phys Rev Lett* **2020**, 125, 117601; b) S. Rahman, H. Saqib, J. Zhang, D. Errandonea, C. Menéndez, C. Cazorla, S. Samanta, X. Li, J. Lu, L. Wang, *Physical Review B* **2018**, 97, 174102; c) C. Cazorla, J. Boronat, *Reviews of Modern Physics* **2017**, 89, 035003.
- [7] Y. Xu, F. Zhang, T. Sheng, T. Ye, D. Yi, Y. Yang, S. Liu, X. Wang, J. Yao, *J Mater Chem A* **2019**, 7, 23191.
- [8] J. Zhang, X. Shang, H. Ren, J. Chi, H. Fu, B. Dong, C. Liu, Y. Chai, *Adv Mater* **2019**, 31, 1905107.
- [9] a) J. Shenoy, J. N. Hart, R. Grau-Crespo, N. L. Allan, C. Cazorla, *Adv Theor Simul* **2019**, 2, 1800146; b) K. Okhotnikov, T. Charpentier, S. Cadars, *Journal of Cheminformatics* **2016**, 8, 17; c) R. Grau-Crespo, S. Hamad, C. R. A. Catlow, N. H. de Leeuw, *Journal of Physics: Condensed Matter* **2007**, 19, 256201; d) R. J. Maurer, C. Freysoldt, A. M. Reilly, J. G. Brandenburg, O. T. Hofmann, T. Björkman, S. Lebègue, A. Tkatchenko, *Annual Review of Materials Research* **2019**, 49, 1.
- [10] a) A. Li, S. Kong, C. Guo, H. Ooka, K. Adachi, D. Hashizume, Q. Jiang, H. Han, J. Xiao, R. Nakamura, *Nat Catal* **2022**, 5, 109; b) C. Hitz, A. Lasia, *Journal of Electroanalytical Chemistry* **2001**, 500, 213.
- [11] K. Momma, F. Izumi, *Journal of Applied Crystallography* **2011**, 44, 1272.
- [12] Z. Chen, C. X. Kronawitter, B. E. Koel, *Phys Chem Chem Phys* **2015**, 17, 29387.
- [13] C. Rong, S. Wang, S. Xin, C. Jia, Q. Sun, Q. Zhang, C. Zhao, *Energ Environ Sci* **2024**, DOI: 10.1039/D4EE00977K.
- [14] N. Wang, P. Ou, R. K. Miao, Y. Chang, Z. Wang, S.-F. Hung, J. Abed, A. Ozden, H.-Y. Chen, H.-L. Wu, J. E. Huang, D. Zhou, W. Ni, L. Fan, Y. Yan, T. Peng, D. Sinton, Y. Liu, H. Liang, E. H. Sargent, *J Am Chem Soc* **2023**, 145, 7829.
- [15] J. Yu, F. A. Garcés-Pineda, J. González-Cobos, M. Peña-Díaz, C. Rogero, S. Giménez, M. C. Spadaro, J. Arbiol, S. Barja, J. R. Galán-Mascarós, *Nat Commun* **2022**, 13, 4341.
- [16] J. Huang, H. Sheng, R. D. Ross, J. Han, X. Wang, B. Song, S. Jin, *Nat Commun* **2021**, 12, 3036.
- [17] W. L. Kwong, C. C. Lee, A. Shchukarev, J. Messinger, *Chem Commun* **2019**, 55, 5017.
- [18] W. L. Kwong, C. C. Lee, A. Shchukarev, E. Björn, J. Messinger, *J Catal* **2018**, 365, 29.
- [19] I. A. Moreno-Hernandez, C. A. MacFarland, C. G. Read, K. M. Papadantonakis, B. S. Brunshwig, N. S. Lewis, *Energ Environ Sci* **2017**, 10, 2103.
- [20] J. S. Mondschein, J. F. Callejas, C. G. Read, J. Y. C. Chen, C. F. Holder, C. K. Badding, R. E. Schaak, *Chem Mater* **2017**, 29, 950.
- [21] X. Yang, H. Li, A.-Y. Lu, S. Min, Z. Idriss, M. N. Hedhili, K.-W. Huang, H. Idriss, L.-J. Li, *Nano Energy* **2016**, 25, 42.